Sub-THz Broadband Transmitting Metasurfaces with Enhanced Frequency Scanning Capability

Li-Zhao Song, Ting Zhang, Pei-Yuan Qin, Jia Du, and Y. Jay Guo

***Abstract*—In this manuscript, broadband transmitting metasurfaces are developed to enhance frequency-dependent beam scanning. A triple-gold-layer unit cell is designed for wideband transmissions with low losses and quasi-linear phase variations. Comprehensive analyses of phase-gradient metasurfaces are provided to enable high-efficiency and wide-angle frequency scanning. For verifications, two metasurfaces with different phase gradients are simulated, manufactured, and measured. Continuous beam scanning performance has been demonstrated successfully from 80 GHz to 220 GHz, showing beam scanning ranges of 25° and 31.5° from two prototypes, respectively. Peak transmission efficiencies of 84% and 75% have been obtained from experiments. The results from simulation and measurement agree very well. The developed metasurfaces have many potential applications such as frequency-scanning terahertz (THz) imaging.**

***Index Terms*— Frequency scanning, transmitting metasurface, THz imaging.**

I. Introduction

Terahertz (THz) waves (from 100 GHz to 10 THz) exhibit numerous unique properties [1]-[2], such as large bandwidth facilitating ultrahigh-data-rate communications, high penetration/transmission through a range of materials and objects, and spectroscopic responses to many materials, etc. Therefore, THz technology holds great potentials in applications for imaging and sensing [3]-[4], biological spectroscopy [5] in addition to wireless communications [6]-[7]. Among these applications, THz imaging is of great importance for non-destructive detections, personnel and object security screening, and surveillance purposes [8]-[9].

The conventional THz imaging systems mostly depend on mechanical scanning, resulting in low frame rates and long processing time [9]. To address this issue, THz frequency-scanning antennas serve as one of the promising candidates [10]-[11], benefiting from the large available spectrum at THz band. They are passive devices that have frequency-dependent beams, i.e., the beam direction varies with frequency. On the other hand, THz phased arrays [12]-[13] and integrated lens antennas [14]-[15] can also provide beam-scanning performances. By using phase-shifting/spatial-shifting mechanisms, their beams can be tuned dynamically in a wide angular range at specific frequencies through external controlling systems. Different from the frequency-scanning antennas, the phased arrays and the integrated lens antennas are both active/reconfigurable devices, which may involve more complicated hardware configurations at the THz band [16]. Therefore, they are typically used in high-end communication and radar systems for wide-angle beam scanning in a relatively narrow operating band [17]. While the frequency-scanning antennas target for low-cost and low-complexity imaging systems, as demonstrated in [18]. This research focuses on developing a new frequency-scanning antenna to facilitate THz imaging applications.

To date, a lot of efforts have been devoted to developing THz leaky-wave antennas due to their frequency-scanning capabilities [19]-[21]. However, transition structures are usually required to connect the feed ports and radiators of the leaky-wave antennas [22]-[23], leading to complicated and costly fabrications. Besides, their radiation efficiencies tend to be low due to propagation losses along the leaky-wave structures. To solve these problems, metasurfaces, composed of judiciously configured two-dimensional (2-D) periodic unit cells, serve as a good candidate for THz frequency scanning [24]-[25] due to their features of flexible beam manipulations [26]. They can provide high directivities with spatial-feeding mechanisms, thus enabling easy implementations and high resolutions.

There are mainly two approaches to design frequency-scanning metasurfaces. The first one is to apply direct pattern synthesis techniques to control its dispersion characteristics [27]-[28]. In [27], the metasurface is assumed to be illuminated by a spherical wave, and its reflecting phase distributions are calculated for far-field synthesis of multiple beams at predefined frequency points. Five beams have been achieved from -5° to -35°, corresponding to five frequency points from 200 GHz to 300 GHz. Despite its flexible and accurate beam synthesis, this design process is only suitable for discrete beam generations at defined frequency points. Another design method of the frequency-scanning metasurface is to employ gradient phase distributions [29]. It can enable continuous beam

Manuscript submitted 28 February 2023, accepted 08 September 2023. This work was supported by Commonwealth Scientific and Industrial Research Organization (CSIRO) Space Technology Future Science Platform Project ST-R2-03. (Corresponding author: Li-Zhao Song.)

Li-Zhao Song, Ting Zhang and Jia Du are with the Manufacturing, Commonwealth Scientific and Industrial Research Organization (CSIRO), Lindfield, NSW, 2070, Australia. (e-mail: Lizhao.Song@csiro.au)

Pei-Yuan Qin and Y. Jay Guo are with the Global Big Data Technologies Centre (GBDTC), University of Technology Sydney (UTS), Ultimo, NSW 2007, Australia. (e-mail: peiyuan.qin@uts.edu.au)

scanning in a defined operating frequency band with planar-wave illuminations. The key design challenge of this approach is that all unit cells need to maintain linear phase variations against frequencies with the same or similar slopes. In this context, there have been some advances for reflecting frequency-scanning metasurfaces [30]-[34]. For example, in [30], a double-mode split-ring unit cell is developed for linear phase variations on the metasurface. A wide beam-scanning range of 40° in a frequency band of 300-500 GHz was obtained with a maximal reflection efficiency of 76%. It should be noted that the reflecting metasurfaces are usually employed when the targets to be identified are in the same half space as the source. On the other hand, transmitting metasurfaces are another good candidate to achieve the frequency-scanning property, and their beam scanning angles can be designed at any desired directions in the forward space. Therefore, they are highly desirable in systems where the targets to be identified are in the other side of the metasurface with respect to the source.

For the transmitting frequency-scanning metasurface, apart from the required linear phase variations, the unit cell should also provide low transmission losses to ensure high efficiencies. Besides, the desired characteristics of transmission amplitude and phase should be consistent in a broad frequency band to enable a wide beam-scanning range. To this end, only few works on the transmitting metasurface have been reported [35]-[37]. In [35], a transmitting binary metasurface is presented, supporting beam scanning in an angular range of 12.5° from 250 GHz to 300 GHz. The peak measured efficiency is 36.5%. In [36], two coding transmitting metasurfaces are designed at 0.8-1.2 THz, showing beam-scanning ranges of 12° and 23° with peak efficiencies of around 67% and 45%, respectively. Moreover, eight cells are developed in [37] with a π/4 phase increment to enable anomalous refraction of a transmitting metasurface. The frequency-scanning functionality is obtained between 0.6-1.8 THz with an angular range of above 20°. The measured peak efficiency is 61%. Even though the beam-scanning ranges and efficiencies in [36]-[37] have been increased, consistent beam radiation patterns are either not investigated or not achieved. This would limit their applications in practical imaging systems.

In this work, broadband transmitting metasurfaces are developed at sub-THz band for high-efficiency and wide-angle frequency-dependent beam scanning. A triple-gold-layer unit cell based on double split rings is proposed to achieve low transmission losses from 115 GHz to 210 GHz. Continuous and quasi-linear phase variations have been obtained in this frequency band by tuning the radii of the two rings. Moreover, with the developed unit cells, comprehensive analyses of different propagation modes in metasurfaces are provided for high-efficiency frequency scanning. Finally, two metasurfaces covering different beam-scanning ranges are designed, fabricated and measured. Good agreement has been observed among theoretical analysis, electromagnetic (EM) simulation and experimental results. The two prototypes can support continuous beam scanning in ranges of 25° and 31.5° with measured peak efficiencies of 84% and 75%, respectively. Compared to other reported transmitting metasurfaces, this work achieves much higher transmission efficiencies with comparable or even larger beam-scanning ranges. Moreover, all the beam patterns show consistent shapes without any distortions.

The rest of the paper is organized as follows. Section II provides details of the developed unit cell model. A comprehensive analysis for frequency-dependent beam-scanning metasurfaces is discussed in Section III. The simulation and measurement results of different prototypes are provided in Section IV. Finally, a conclusion is drawn in Section V.

II. Unit Cell Design

As sketched in Fig. 1, the metasurface studied consists of a number of unit cells with different transmission phases along y-axis. They have a constant phase gradient of δ. For each column along x-axis, the unit cells have the same transmission phase. The physical periodicity of the unit cell is marked as P. Its radiation array factor along *yoz* plane can be obtained as

$$F_1(\theta) = \sum_{q=1}^{Q} E_q e^{-j(q-1)kPsin\theta_i} e^{j(q-1)(kPsin\theta+\delta)}, \quad (1)$$

where Q is the total number of the unit cell, k is the propagation constant in free space, θ_i is the angle of incident wave, E_q is the illumination amplitude of the *q-th* unit cell.

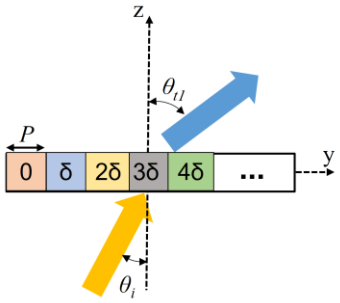

Fig. 1 Schematic of a transmitting metasurface with a constant phase gradient.

Considering a uniform illumination (E_q=1) and each unit cell radiates as an ideal point source, the transmitted beam angle θ_{t1} can be calculated as

$$\theta_{t1} = \arcsin\left(\sin\theta_i - \frac{\delta+2n\pi}{2\pi Pf}c\right), \text{n=0, ±1, ±2, …} \quad (2)$$

where f is the operating frequency, c is the free-space light speed, and n represents different mode order.

It can be noticed that the transmitted beam will scan continuously with respect to frequency if the phase gradient δ is independent of frequency. Therefore, the unit cells should have linear phase variations with the same or similar slopes. To achieve a wide operating bandwidth for a large scanning range, one would need to develop broadband transmitting unit cells with linearly variable transmission phases.

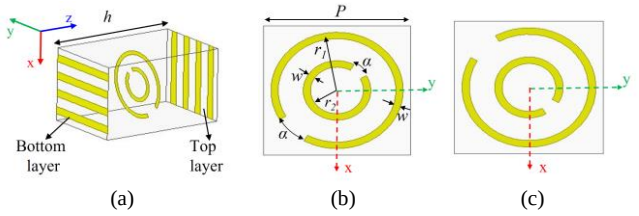

Fig. 2 Unit cell model. (a) 3-D view. (b) Model 1. (c) Model 2.

To meet the abovementioned requirements, a triple-gold-layer unit cell is developed on the substrate of Rogers RT/duroid 5880 (ε_r=2.3, tan δ=0.02 at 200 GHz [38]). As shown in Fig. 2 (a), the unit cell is composed of two asymmetric concentric rings sandwiched by two orthogonally configured strip arrays. The gold is represented by yellow color. The strips on bottom layer are along y-axis, enabling wideband x-polarised transmission and y-polarised reflection. The middle layer functions as a polarisation convertor, i.e., the x-polarised wave from the bottom layer would be converted into y-polarised one. The strips on top layer are along x-axis, transmitting y-polarised waves and reflecting x-polarised ones. As discussed in [39], this configuration can support broadband and high-efficiency transmissions due to Fabry-Perot-like resonances inside it.

In our model, the middle layer for polarisation conversions is designed with considerations of both broadband transmissions and linear phase tuneability. It is composed of notched double rings with the same notch angle α yet different notched positions, as illustrated in Fig. 2 (b). The radii of the two rings are r_1 and r_2, respectively. The widths of both rings are the same as w. The notch on the outer ring is at -45° with respect to x-axis, while the notch on the inner ring is at 135°. This structure is denoted as Model 1. All parameters of this unit cell model are listed here: P=1 mm, h=0.508 mm, w=0.05mm, r_1=0.4 mm, r_2=0.18 mm. 3-D EM simulation software ANSYS HFSS is applied for unit cell analyses. Two pairs of periodic boundaries are assigned along x- and y-axes, respectively. Two Floquet ports are added along z-axis. For each port, two zeroth-order orthogonal Floquet modes have been employed for analyses, namely TM_{00} and TE_{00} modes. They correspond to y-polarised and x-polarised planar incident waves, respectively. We use a single frequency meshing at 200 GHz under adaptive meshing solution in HFSS. The maximum delta S is set as 0.005 to measure the solution error and the maximum number of passes is set as 15 to ensure the solution finishes. A frequency sweep between 80 GHz and 230 GHz is added to assess the properties in the investigated bandwidth. The substrate material is defined with ε_r=2.3, tan δ=0.02. Two reference planes are applied at the top and bottom interfaces of the unit cell for S-parameter characterizations.

To enable phase variations, we tune the radii of the two rings simultaneously. The notch angle α is chosen as a fixed value of 30°. The radii of the two rings are variables related to a factor ks, that is, r_1=0.4ks mm, r_2=0.18ks mm. The transmission phase can be tuned by varying the value of ks. The simulated transmission amplitudes and phases of Model 1 are plotted in Fig. 3 with the factor ks varied from 0.7 to 1. The transmission bandwidth for a greater than -3 dB amplitude is from 117 GHz to 165 GHz, and it is from 115 GHz to around 210 GHz for a greater than -5 dB amplitude. Besides, the transmission phases of different unit cells show quasi-linear responses to the frequency with similar slopes. At the frequency of 155 GHz, the phase range from Model 1 is -224°~-45°, covering 180°. To enable a 360° full phase tuning range, Model 1 is flipped along y-axis, producing another structure (Model 2) as shown in Fig. 2 (c). The simulated transmission coefficients of Model 2 are shown in Fig. 3. Compared to the unit cell of Model 1 with the same physical parameter ks, the transmission phase of Model 2 shows a 180° difference, without changing the transmission amplitude. This way, broadband transmitting unit cells have been realised with quasi-linear phase variations in a range of 360°. The slopes of different phase curves in Fig. 3 remain constant when ks changes, promising the frequency-scanning capability of a transmitting metasurface. This stable phase response is attributed to the designed middle metallic structure of the unit cell and the accompanied phase-tuning mechanism. Besides, for each curve, the phase value decreases with frequency monotonically in the corresponding transmission band, showing dispersive responses. This is due to the Fabry-Perot resonance.

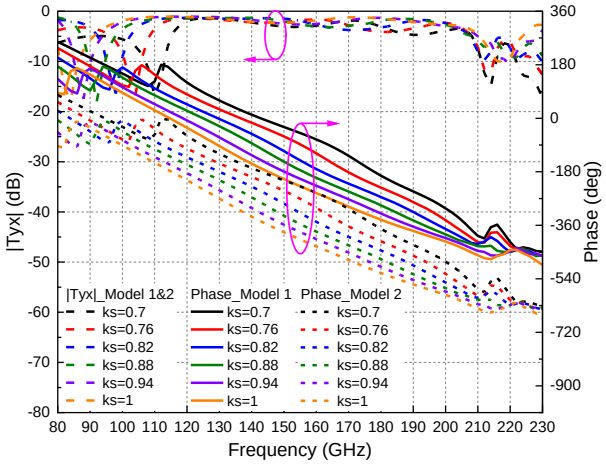

Fig. 3 Simulated transmission coefficients of the final design from both Model 1 and 2.

III. Frequency-Dependent Beam-Scanning Mechanism

Based on the developed unit cell in Section II, beam scanning responses of phase-gradient metasurfaces with respect to different frequencies are investigated. Denoting the metasurface configuration in Fig. 1 as Array A, under normal illuminations (θ_i=0), its transmitted beam angle can be calculated from (2). Beam angles of the fundamental mode (n=0) versus frequency for different phase gradients δ are shown in Fig. 4. It is found that a larger value of δ can provide a larger beam scanning range in a fixed frequency band. However, as shown in Fig. 4, when δ is greater than $\pi/2$, the first negative harmonic mode would appear and incur grating lobes, resulting in a low transmission efficiency of the main scanning beam. Therefore, in order to obtain a large beam scanning range without sacrificing the transmission efficiency, the phase

gradient should satisfy $\delta \leq \pi/2$ and the unit cell should have a broad operating bandwidth.

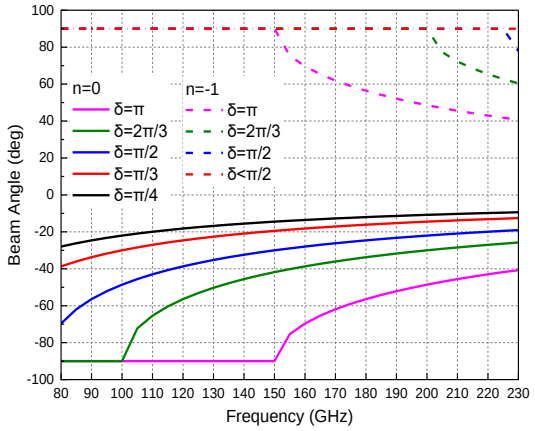

Fig. 4 Transmitted beam angles of Array *A* versus frequency for different phase gradients and different modes.

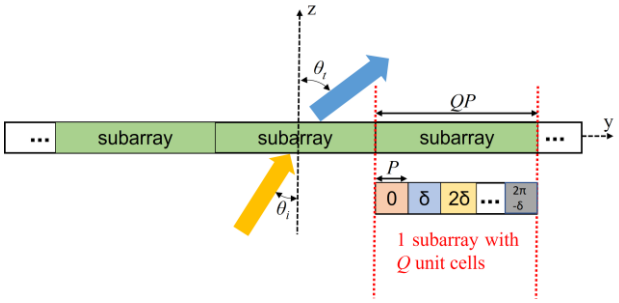

Fig. 5 Schematic of a transmitting metasurface including periodic subarrays.

Metasurfaces are usually designed with large electrical dimensions for high gains and narrow beamwidths. Based on the above analysis, it is not advisable to design a frequency-scanning metasurface with a large number of unit cells within only one phase cycle (0-2π), as the phase gradient δ would be too small and the scanning capability would be weakened significantly. Therefore, the metasurface usually consists of several subarrays with repetitive phase cycles. As shown in Fig. 5, each subarray contains *Q* unit cells covering one phase cycle, i.e., $Q\delta=2\pi$. For clarity, the configuration of the whole metasurface including several periodic subarrays with a periodicity of *QP* is denoted as Array *B*. Considering Array *B* with *S* repetitive subarrays, its radiation array factor is calculated as

$$F_2(\theta) = \sum_{s=1}^{S} E_s e^{-j(s-1)kQP\sin\theta_i} e^{j(s-1)(kQP\sin\theta)}, \quad (3)$$

where E_s represents the illumination amplitude of the *s-th* subarray. Under uniform illuminations (E_s=1), the transmitted beam angle θ_{t2} can be calculated as

$$\theta_{t2} = \arcsin\left(\sin\theta_i - \frac{m\delta}{2\pi Pf}c\right), \text{ m=0, ±1, ±2, …} \quad (4)$$

which contains different harmonic modes denoted by *m*.

From (4), it is observed that Array *B* configuration also supports frequency-dependent beam scanning under higher order modes (when $m\neq0$). As examples, Fig. 6 (a) and (b) show the transmitted beam angles of positive 1st and 2nd harmonic modes versus frequency for different values of δ, respectively. Similar to Array *A*, the larger value of δ is, the larger beam scanning range can be obtained in a fixed frequency band.

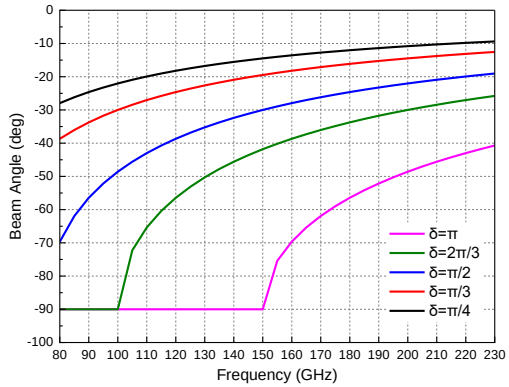

(a)

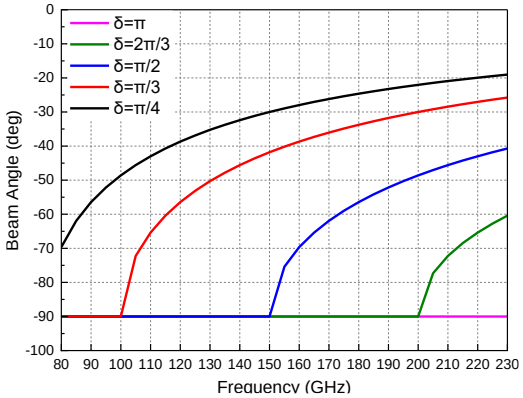

(b)

Fig. 6 Transmitted beam angles of Array *B* versus frequency for different phase gradients. (a) Beam of *+1st* harmonic mode (*m*=1). (b) Beam of *+2nd* harmonic mode (*m=2*).

For the whole metasurface in Fig. 5 with considerations of both Array *A* and *B* configurations, its radiation pattern should follow

$$F_{meta}(\theta) = |F_1(\theta)F_2(\theta)|. \quad (5)$$

Consequently, the scanning efficiency will be enhanced if the scanning beams from Array *A* and *B* can overlap with each other, i.e., $\theta_{t1}= \theta_{t2}$. Considering (2) and (4), one can obtain

$$m = 1 + \frac{2\pi n}{\delta}. \quad (6)$$

One of the solutions for (6) is *m*=1 and *n*=0. This implies that the *+1st* order mode of (4) agrees with the fundamental mode of (2) regardless of the phase gradient δ. Another solution for (6) is *m=-1* and *n=-1* only when the phase gradient is $\delta=\pi$. However, in this case, the beam from *m*=1 and *n*=0 also exists, which will reduce the transmission powers of main beams.

IV. Prototype Simulation and Measurement

A. Metasurface Simulations

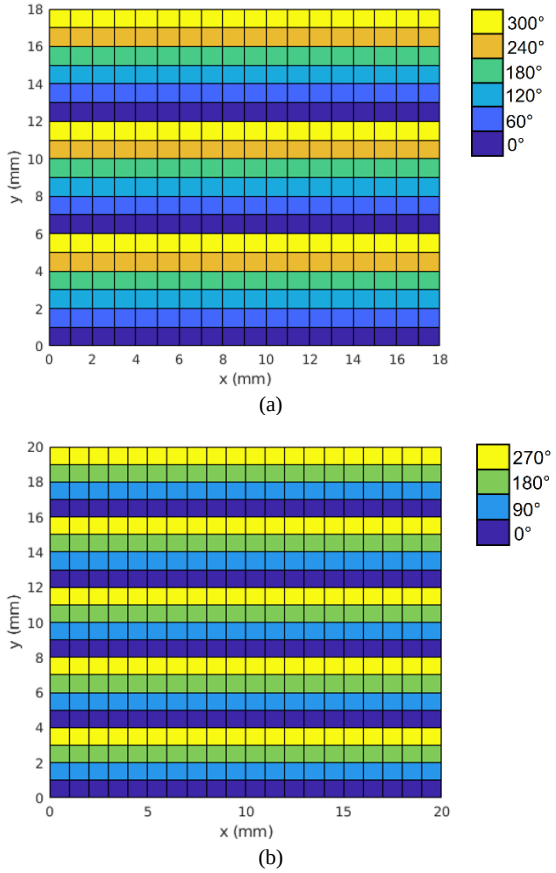

Fig. 7 Phase distributions on the two designed metasurfaces. (a) Meta. I. (b) Meta. II.

Based on the previous analysis, to enable a high scanning efficiency, the fundamental mode of (2) should be chosen as the main scanning beam, which coincides with the $+1^{st}$ order mode of (4). Meanwhile, referring to Fig. 4, it is noticed that the higher order mode of (2) can be eliminated if the phase gradient satisfies $\delta<=\pi/2$, thereby improving the main beam transmission efficiency further. Besides, the larger δ is, the wider beam coverage can be obtained. In this context, to demonstrate the frequency scanning capability in different angular ranges with high efficiencies, two metasurfaces Metas. I and II are investigated with phase gradients δ as $\pi/3$ and $\pi/2$, respectively. Following the configuration in Fig. 5, the subarrays of these two metasurfaces should contain six and four unit cells to cover a 2π range, respectively. The unit cell presented in Section II is utilized for modelling. For Meta. I, it has a dimension of 18 mm×18 mm with 18×18=324 unit cells. The whole metasurface includes 3 subarrays along *y*-axis, where each subarray consists of 6 unit cells with a phase gradient of $\pi/3$. Its phase distribution is shown in Fig. 7 (a). For Meta. II, it has a dimension of 20 mm×20 mm with 20×20=400 unit cells. The whole metasurface includes 5 subarrays along *y*-axis, where each subarray consists of 4 unit cells with a phase gradient of $\pi/2$. The corresponding phase distribution is given in Fig. 7 (b). Unit cell models with the desired transmission phases from Section II are applied to implement the two metasurfaces. Gaussian beams in HFSS are assigned to illuminate them. The beam waists are calculated based on the experimental setup, with beam diameters of 22.3 mm, 25.5 mm and 26.7 mm in the three frequency bands of 80-110 GHz, 110-170 GHz, and 170-220 GHz, respectively. Far-field radiation patterns are simulated and given in Fig. 9 (a) and (b) for Meta. I and II, respectively. It can be observed that the scanning range of Meta. I is realised from -38° at 80 GHz to -13° at 220 GHz. For Meta. II, the beam is scanning from -51.5° at 94 GHz to -20° at 220 GHz. Please note that the beam of Meta. II at 80 GHz is not discussed here due to its large radiation angle and being close to surface waves.

B. Fabrication and Measurement

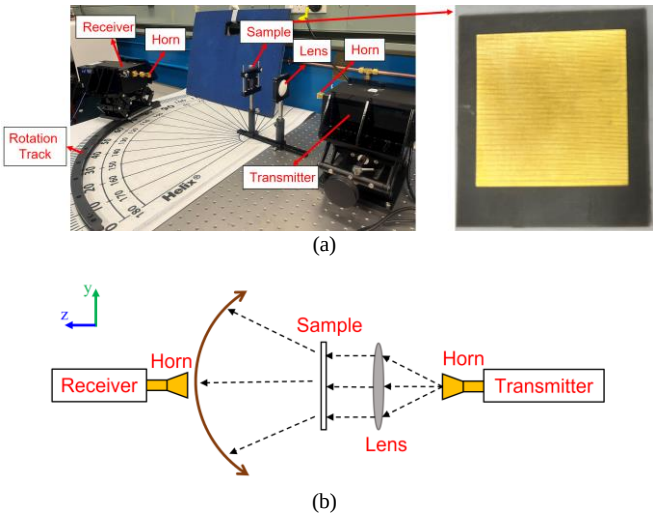

Fig. 8 (a) Photograph of one fabricated prototype and measurement setup. (b) Diagram of the measurement setup.

As a proof of concept, the aforementioned two metasurfaces have been fabricated and measured. Each metasurface consists of two laminated substrates of Rogers RT/duroid 5880. Each substrate has a thickness of 0.254 mm. The gold patterns on the substrates are realised using laser etching technology. The pictures of one sample and the measurement setup are shown in Fig. 8 (a). A schematic diagram of the experimental setup is shown in Fig. 8 (b). The sample is positioned at the center of a circular track with a radius of 0.5 m, while the receiver antenna moves along the arc for measurements at different angles. 0.5 m is at the far field for Meta. I from 80 GHz to 220 GHz. It is at the far field for Meta. II at frequencies lower than 190 GHz, and is at the edge of far field and Fresnel region at frequencies greater than 190 GHz. We used the track with a 0.5 m radius (the only track available in our lab) to measure the radiation patterns for both metasurfaces from 80 GHz to 220 GHz. A collimated beam is generated at the transmitter end at various frequencies and radiates to the metasurface, then the transmitted power is detected by the receiver for efficiency and pattern measurements. Multiple frequency extenders are applied to the transmitter and receiver to cover the wide frequency range for measurement.

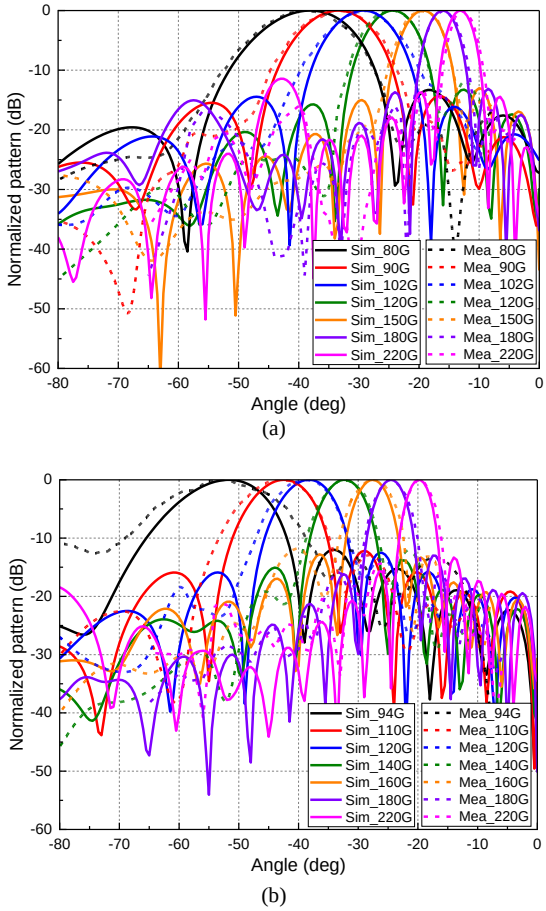

Fig. 9 Simulated and measured normalized radiation patterns. (a) Meta. I. (b) Meta. II.

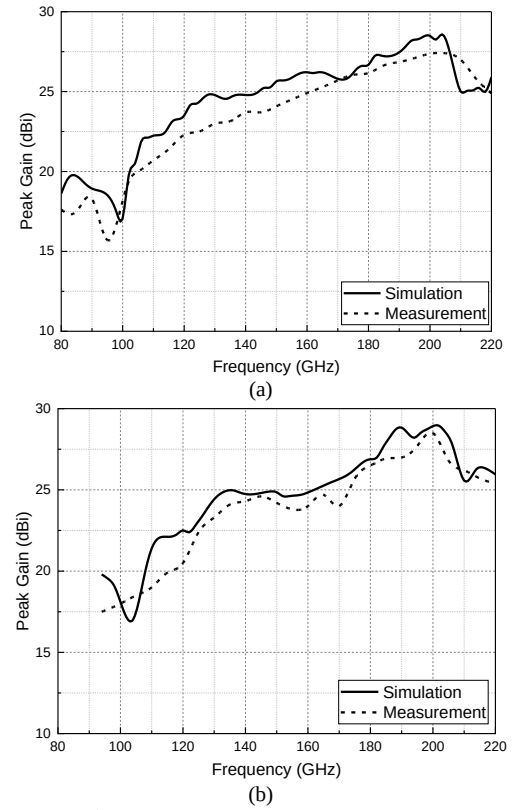

Fig. 10 Peak gains from simulation and measurement. (a) Meta. I. (b) Meta. II.

The measured far-field radiation patterns of the two prototypes are normalized and compared with the simulated ones in Fig. 9 (a) and (b), respectively. Good agreement between simulation and measurement can be observed. There are only less than 1° differences in terms of 3-dB beamwidths from simulation and measurement, except for Meta. II at 94 GHz, where a slightly wider beamwidth than the simulated counterpart is found. The simulated and measured peak gains have been compared in Fig. 10. It is noticed that the results from simulation and measurement agree reasonably well. The peak gain continuously increases with frequency. This agrees with the property of frequency-scanning antennas, as the electrical size of the antenna aperture becomes larger when the frequency increases. It has measured 3-dB gain bandwidths of 34.7% from 155 GHz to 220 GHz for Meta. I and 22.8% from 175 GHz to 220 GHz for Meta. II, respectively.

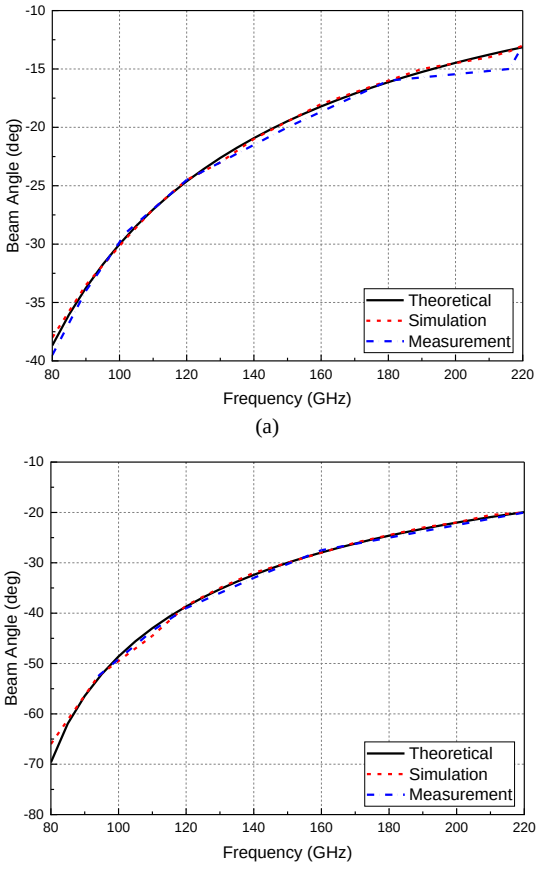

Fig. 11 Main beam angles versus frequency from theoretical analysis, 3-D simulation and measurement. (a) Meta. I. (b) Meta. II.

Moreover, the main beam angles of the two prototypes versus frequency are plotted in Fig. 11 in terms of the results from theoretical analysis, EM simulation and measurement. They agree with each other very well. Besides, the transmission efficiency is calculated as the ratio of the transmitted power at the scanned angle and the measured reference power with a same-size hollow copper film. The measured transmission efficiencies of the two prototypes versus frequency are shown in Fig. 12. The peak efficiencies are obtained as 84% and 75% for Metas. I and II, respectively. It is noticed that the

transmission efficiencies at the bands of 85-110 GHz and 200-220 GHz are low. This is due to the high transmission losses of the metasurface unit cell and the phase deviations from the ideal linear response at these frequencies.

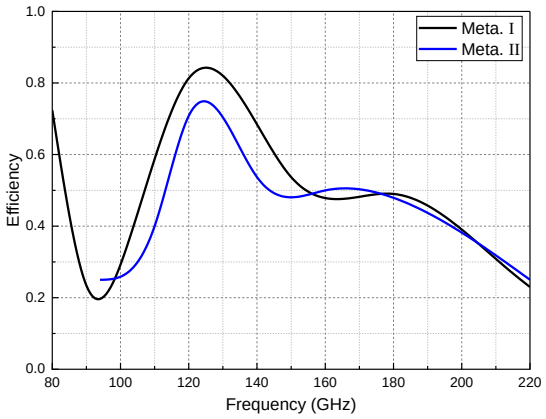

Fig. 12 Measured transmission efficiencies of the two prototypes versus frequency.

A comparison is conducted in Table I to visualize the frequency-scanning performances of this work and other reported THz transmitting metasurfaces. It is noticed that continuous beam scanning with stable radiation patterns in wide angular ranges has been achieved from the two developed metasurfaces, providing higher peak and average transmission efficiencies than other works. The higher efficiencies of the reported metasurfaces are obtained due to the employment of specifically determined mode orders and phase gradients. Furthermore, the relatively wide beam angular range is attributed to the developed broadband transmitting unit cell with quasi-linear phase variations. Compared to other designs, it has lower transmission losses and better linear phase responses in a much wider bandwidth, thus enabling a larger frequency-scanning range. Please note that the operating frequency band of 80-220 GHz is chosen considering the minimum dimensions of the employed unit cells for low-cost fabrications. This operating bandwidth is defined for achieving stable frequency-scanning beams with low sidelobes and non-distorted radiation patterns, which is consistent with the standard employed in other references in Table I. The design concepts for unit cells and metasurfaces can be applied to higher frequency bands.

TABLE I
FREQUENCY-SCANNING PERFORMANCES FROM DIFFERENT TRANSMITTING METASURFACES

Ref.	Operating frequency (GHz)	Beam scanning range	Efficiency (%)	3-dB gain bandwidth (%)	Continuous beam scanning
[28]	225-325	14.3°	/	22.5	No
[35]	250-300	12.5°	20-36.5	/	Yes
[36]	800-1200	12°/23°	27-67	/	Yes
[37]	600-1800	>20°	30-61	/	Yes
This work	80-220	25°/31.5°	20-84	34.7/22.8	Yes

V. CONCLUSION

Transmitting metasurfaces for high-efficiency wide-angle beam scanning with respect to frequencies are discussed. Broadband unit cells are designed for low transmission losses and quasi-linear phase responses. Different harmonic modes are analysed in frequency-scanning metasurfaces, facilitating high-efficiency and wide-angle beam scanning. Two prototypes with different configurations have been manufactured and tested, showing good agreement with simulation results. Wide beam-scanning ranges of 25° and 31.5° have been obtained from the two prototypes respectively in a frequency band of 80-220 GHz. In addition, peak transmission efficiencies have been realised as 84% and 75% from the two prototypes, respectively. The proposed design methods for transmitting frequency-scanning metasurfaces can be applied in advanced THz imaging systems. It should be noted that the current frequency scanning is only realised in one direction, and mechanical movement is still needed in another direction for imaging. More research efforts will be devoted to exploring 2-D frequency-scanning capability in our future research.

ACKNOWLEDGEMENT

The authors would like to thank Associate Professor Yang Yang from University of Technology Sydney for his contributions on the configuration and establishment of the measurement platform.

REFERENCES

[1] Z. Popovic and E. N. Grossman, “THz metrology and instrumentation,” *IEEE Trans. Thz Sci Technol.* vol. 1, no. 1, pp. 133-144, Sep. 2011.
[2] M. Tonouchi, “Cutting-edge terahertz technology,” *Nat. Photonics*, vol. 1, no. 2, pp. 97-105, Feb. 2007.
[3] J. F. Federici, B. Schulkin, F. Huang, D. Gary, R. Barat, F. Oliveira, and D. Zimdars, “THz imaging and sensing for security,” *Semicond. Sci. Technol.*, vol. 20, no. 7, pp. S266–S280, 2005.
[4] S. Gu, C. Li, X. Gao, Z. Sun, and G. Fang, “Terahertz aperture synthesized imaging with fan-beam scanning for personnel screening,” *IEEE Trans. Microw. Theory Techn.*, vol. 60, no. 12, pp. 3877–3885, Dec. 2012.
[5] Y. Cao, P. Huang, X. Li, W. Ge, D. Hou, and G. Zhang, “Terahertz spectral unmixing based method for identifying gastric cancer,” *Phys. Med. Biol.*, vol. 63, no. 3, 2018.
[6] H.-J. Song and T. Nagatsuma, “Present and future of terahertz communications,” *IEEE Trans. Terahertz Sci. Technol.*, vol. 1, no. 1, pp. 256–263, Sep. 2011.
[7] T. Harter, C. Füllner, J. N. Kemal, S. Ummethala, and C. J. N. P. Koos, “Generalized Kramers–Kronig receiver for coherent terahertz communications,” *Nat. Photon.*, vol. 14, no. 10, pp. 601–606, Oct. 2020.
[8] R. Appleby and H. B. Wallace, “Standoff detection of weapons and contraband in the 100 GHz to 1 THz region,” *IEEE Trans. Antennas Propag.*, vol. 55, no. 11, pp. 2944–2956, Nov. 2007.
[9] K. B. Cooper, R. J. Dengler, N. Llombart, B. Thomas, G. Chattopadhyay and P. H. Siegel, “THz imaging radar for standoff personnel screening,” *IEEE Trans. Terahertz Technol.*, vol. 1, no. 1, pp. 169–182, Sep. 2011.
[10] Y. Álvarez, R. Camblor, C. Garcia, J. Laviada, C. Vázquez, S. Ver-Hoeye, G. Hotopan, M. Fernández, A. Hadarig, A. Arboleya, and F. Las-Heras, “Submillimeter-wave frequency scanning system for imaging applications,” *IEEE Trans. Antennas Propag.*, vol. 61, no. 11, pp. 5689-5696, Nov. 2013.
[11] Y. Alvarez, C. Garcia Gonzalez, C. Vazquez Antuna, S. Ver-Hoeye and F. Las-Heras, “Measurement setup for imaging applications using frequency scanning illumination,” *IEEE Trans. Instrum. Meas.*, vol. 61, no. 11, pp. 3014-3023, Nov. 2012.
[12] K. Guo, Y. Zhang and P. Reynaert, “A 0.53-THz subharmonic injection-locked phased array with 63-μW radiated power in 40-nm CMOS,” *IEEE J. Solid-State Circuits*, vol. 54, no. 2, pp. 380-391, Feb. 2019.

[13] R. Klimovich, S. Jameson and E. Socher, "W-Band endfire 2-D phased-array transmitter based on ×9 CMOS active multiplier chips," *IEEE Trans. Antennas Propag.*, vol. 68, no. 12, pp. 7893-7904, Dec. 2020.
[14] M. Alonso-delPino, C. Jung-Kubiak, T. Reck, N. Llombart and G. Chattopadhyay, "Beam scanning of silicon lens antennas using integrated piezomotors at submillimeter wavelengths," *IEEE Trans. Terahertz Sci. Technol.*, vol. 9, no. 1, pp. 47-54, Jan. 2019.
[15] S. Bosma, N. v. Rooijen, M. Alonso-delPino, M. Spirito and N. Llombart, "W-Band demonstration of dynamic, high-gain beam steering with a scanning lens phased array," *2022 47th International Conference on Infrared, Millimeter and Terahertz Waves (IRMMW-THz)*, pp. 1-2, Delft, Netherlands, 2022.
[16] J. C. Balzer, C. J. Saraceno, M. Koch, P. Kaurav, U. R. Pfeiffer, W. Withayachumnankul, T. Kürner, A. Stöhr, M. El-Absi, A. A. H. Abbas, T. Kaiser, and A. Czylwik, "THz systems exploiting photonics and communications technologies," *IEEE J. Microwaves*, 2022.
[17] Y. J. Guo, and R. W. Ziolkowski, "Advanced antenna array engineering for 6G and beyond wireless communications," *John Wiley & Sons*, 2021.
[18] S. Li, C. Li, W. Liu, Z. Sun, S. Lang, Z. Lu, X. Zhang, and G. Fang, "Study of terahertz superresolution imaging scheme with real-time capability based on frequency scanning antenna," *IEEE Trans. Terahertz Sci. Technol.*, vol. 6, no. 3, pp. 451-463, May 2016.
[19] A. Basu and T. Itoh, "Dielectric waveguide-based leaky-wave antenna at 212 GHz," *IEEE Trans. Antennas Propag*., vol. 46, no. 11, pp. 1665-1673, Nov. 1998.
[20] S. S. Yao, Y. J. Cheng, Y. F. Wu and H. N. Yang, "THz 2-D frequency scanning planar integrated array antenna with improved efficiency," *IEEE Antennas Wirel. Propag. Lett.*, vol. 20, no. 6, pp. 983-987, Jun. 2021.
[21] A. Gomez-Torrent, M. García-Vigueras, L. L. Coq, A. Mahmoud, M. Ettorre, R. Sauleau, and J. Oberhammer, "A low-profile and high-gain frequency beam steering subterahertz antenna enabled by silicon micromachining," *IEEE Trans. Antennas Propag.*, vol. 68, no. 2, pp. 672-682, Feb. 2020.
[22] U. Dey, J. Tonn and J. Hesselbarth, "Millimeter-wave dielectric waveguide-based leaky-wave antenna array," *IEEE Antennas Wirel. Propag. Lett*., vol. 20, no. 3, pp. 361-365, Mar. 2021.
[23] E. D. Cullens, L. Ranzani, K. J. Vanhille, E. N. Grossman, N. Ehsan and Z. Popovic, "Micro-fabricated 130–180 GHz frequency scanning waveguide arrays," *IEEE Trans. Antennas Propag*., vol. 60, no. 8, pp. 3647-3653, Aug. 2012.
[24] S. Liu, T. J. Cui, L. Zhang, Q. Xu, Q. Wang, X. Wan, J. Q. Gu, W. X. Tang, M. Q. Qi, J. G. Han, W. L. Zhang, X. Y. Zhou, and Q. Cheng, "Convolution operations on coding metasurface to reach flexible and continuous controls of terahertz beams," *Adv. Sci.*, vol. 3, no. 10, p. 1600156, Jul. 2016.
[25] X. Zhang, Z. Tian, W. Yue, J. Gu, S. Zhang, J. Han, and W. Zhang, "Broadband terahertz wave deflection based on C-shape complex metamaterials with phase discontinuities," *Adv. Mater.*, vol. 25, no. 33, pp.4567-4572, Sep. 2013.
[26] C. L. Holloway, E. F. Kuester, J. A. Gordon, J. O'Hara, J. Booth and D. R. Smith, "An overview of the theory and applications of metasurfaces: the two-dimensional equivalents of metamaterials," *IEEE Antennas Propag. Mag.*, vol. 54, no. 2, pp. 10-35, Apr. 2012.
[27] S.-W. Qu, W.-W. Wu, B.-J. Chen, H. Yi, X. Bai, K. B. Ng, and C. H. Chan, "Controlling dispersion characteristics of terahertz metasurface." *Sci. Rep.*, vol. 5, no. 1, pp. 1-6, Mar. 2015.
[28] H. Yi, S.-W. Qu, K.-B. Ng, C. H. Chan and X. Bai, "3-D printed millimeter-wave and terahertz lenses with fixed and frequency scanned beam," *IEEE Trans. Antennas Propag.*, vol. 64, no. 2, pp. 442-449, Feb. 2016.
[29] N. Yu, P. Genevet, M. A Kats, F. Aieta, J.-P. Tetienne, F. Capasso, Z. Gaburro, "Light propagation with phase discontinuities: generalized laws of reflection and refraction," *Science*, vol. 334, no. 6054, pp. 333-337, Oct. 2011.
[30] H. Zeng, F. Lan, Y. Zhang, T. Song, S. Liang, L. Wang, T. Zhang, L. Wang, Z. Shi, X. Zhang, P. Mazumder, and Z. Yang, "Maximizing beam-scanning angle in an expected bandwidth based on terahertz metasurface with dual-mode resonance," *Appl. Phys. Express*, vol. 12, no. 9, p. 095501, Aug. 2019.
[31] S. Zheng, C. Li, S. Li, X. Zhang, and G. Fang, "Realizing frequency controlled wide-angle beam scanning with an artificial electromagnetic structure in the terahertz band," *Opt. Express*, vol. 26, no. 14, pp. 18532-18544, Jul. 2018.
[32] S. Li, C. Li, X. Zhang and G. Fang, "A planar binary structure for realizing frequency controlled beam-steering at 0.2-terahertz band," *IEEE Antennas Wirel. Propag. Lett.*, vol. 13, pp. 1007-1010, 2014.
[33] S. Li, C. Li, X. Zhang, and G. Fang, "Achievement of beam steering in terahertz band based on frequency-scanning grating-reflector antenna," *Electron. Lett.*, vol. 50, no. 3, pp. 136-138, Jan. 2014.
[34] B. Xiao, F. Lan, Z. Yang, P. Mazumder, Z. Shi, Y. Xu, H. Zeng, and J. Yin, "Broadband and high-efficiency circular-polarized terahertz frequency scanning metasurface," *IEEE Photonics & Electromagnetics Research Symposium-Fall (PIERS-Fall)*, pp. 3229-3231, Dec. 2019.
[35] S. Zheng, C. Li, S. Wu, H. Li, G. Yang, and G. Fang, "Terahertz transmissive metasurface for realizing beam steering by frequency scanning," *J. Light. Technol.*, vol. 39, no. 17, pp. 5502-5507, Sep. 2021.
[36] S. Liu, A. Noor, L. L. Du, L. Zhang, Q. Xu, K. Luan, T. Q. Wang, Z. Tian, W. X. Tang, J. G. Han, W. L. Zhang, X. Y. Zhou, Q. Cheng, and T. J. Cui, "Anomalous refraction and nondiffractive Bessel-beam generation of terahertz waves through transmission-type coding metasurfaces." *ACS Photonics*, vol.3, no. 10, pp. 1968-1977, Oct. 2016.
[37] N. K. Grady, J. E. Heyes, D. R. Chowdhury, Y. Zeng, M. T. Reiten, A. K. Azad, A. J. Taylor, D. A. R. Dalvit, H.-T. Chen, "Terahertz metamaterials for linear polarization conversion and anomalous refraction," *Science*, vol. 340, no. 6138, pp. 1304-1307, Jun. 2013.
[38] K. B. Ng, and C. H. Chan, "On the dielectric properties of substrates with different surface conditions for submillimeter-wave and terahertz applications," *THz Sci. Technol.*, vol. 9, no. 2, pp. 45-59, Jun. 2016.
[39] D. Y. Liu, M. H. Li, X. M. Zhai, L. F. Yao, and J. F. Dong, "Enhanced asymmetric transmission due to Fabry-Perot-like cavity," *Opt. Express*, vol. 22, no. 10, pp. 11707-11712, May 2019.

Li-Zhao Song (Member, IEEE) was born in Xianyang, Shaanxi, China, in 1996. She received the bachelor's degree in electronic and information engineering from Xidian University, Xi'an, in 2016, and the Ph.D. degree from University of Technology Sydney (UTS), Australia, in 2022.

Since July 2021, she has been working as a Post-Doctoral Research Fellow with the Manufacturing Business Unit of Commonwealth Scientific and Industrial Research Organization (CSIRO), Lindfield, NSW, Australia. Her research interests include transmitarray antennas, lens antennas and meta-surface antennas.

Ting Zhang received his Bachelor Degree in electronics engineering and information science from University of Science and Technology of China (UTSC), China, in 2007, and a Ph.D. degree in Microelectronics and solid-state electronics from University of Chinese Academy of Science in 2013. He was a Postdoctoral Research Fellow with the Commonwealth Scientific and Industrial Research Organisation (CSIRO), Australia from 2013 to 2016, and a Chancellor's Postdoctoral Research Fellow with the Global Big Data Technology Center (GBDTC), University of Technology Sydney (UTS) from 2017 to 2022. Since 2022, he has been a senior research scientist in CSIRO.

Pei-Yuan Qin (Senior Member, IEEE) received a joint Ph.D. Degree from Xidian University, China and Macquarie University, Australia, in 2012. He is now an Associate Professor with University of Technology Sydney, Australia. His research interests are in the areas of reconfigurable antennas, antenna arrays, and microwave components. Dr. Qin was a recipient of an Australia Research Council Discovery Early Career Researcher Award.

Jia Du received the B.S. from Xidian University, China, in 1982, M.S. from University of Electronic Science and Technology of China in 1984, and the Ph.D. from University of Technology, Sydney, Australia, in 1993. She has been working in Australian Commonwealth Scientific and Industrial Research Organisation (CSIRO) since 1995 and is currently a Senior Principal Research Scientist.

Dr Du has extensive research experience in a broad range of interdisciplinary areas of semiconductor and superconductor electronic devices as well as 2D material-based devices and the application systems. She has led the CSIRO capability development of high-Tc superconducting (HTS) Josephson junction-based quantum sensors, including superconducting quantum interference devices (SQUIDs), microwave, millimetre wave and terahertz devices and circuits, and their applications in mineral exploration, terahertz imaging, millimetre wave and terahertz wireless communication systems. She also leads CSIRO new capability development of terahertz metasurfaces and graphene-based tuneable/reconfigurable electronic devices. She has published more than 230 research papers including 110 peer-reviewed journal papers with over 2340 citations.

Y. Jay Guo (Fellow, IEEE) received a Bachelor's Degree and a Master's Degree from Xidian University in 1982 and 1984, respectively, and a Ph.D Degree from Xian Jiaotong University in 1987, all in China. His current research interests include 6G antennas, mm-wave and THz communications and sensing systems as well as big data technologies. He has published five books and over 700 research papers including over 340 IEEE Transactions papers, and he holds 26 international patents.

Jay is a Fellow of the Australian Academy of Engineering and Technology and a Fellow of IEEE. He was a member of the College of Experts of Australian Research Council (ARC, 2016-2018). Jay has won a number of the most prestigious Australian national awards including the Engineering Excellence Awards (2007, 2012) and CSIRO Chairman's Medal (2007, 2012). He was named one of the most influential engineers in Australia in 2014 and 2015, and Australia's Research Field Leader in Electromagnetism by the Australian Research Report for four consecutive years since 2020. Together with his students and postdocs, he has won numerous best paper awards. In 2023, Jay received the prestigious IEEE APS Sergei A. Schelkunoff Transactions Paper Prize Award.

Jay is a Distinguished Professor and the Director of Global Big Data Technologies Centre (GBDTC) at the University of Technology Sydney (UTS), Australia. He is the founding Technical Director of the New South Wales (NSW) Connectivity Innovation Network (CIN). Prior to joining UTS in 2014, Prof Guo served as a Director in CSIRO for over nine years. Before joining CSIRO, he held various senior technology leadership positions in Fujitsu, Siemens and NEC in the U.K.

Jay has chaired numerous international conferences and served as a guest editor for a number of IEEE publications. He was the Chair of International Steering Committee, International Symposium on Antennas and Propagation (2019-2021). He has been the International Advisory Committee Chair of IEEE VTC2017, General Chair of ISAP2022, ISAP2015, iWAT2014 and WPMC'2014, and TPC Chair of 2010 IEEE WCNC, and 2012 and 2007 IEEE ISCIT. He served as Guest Editor of special issues on "Low-Cost Wide-Angle Beam Scanning Antennas", "Antennas for Satellite Communications" and "Antennas and Propagation Aspects of 60-90GHz Wireless Communications," all in IEEE Transactions on Antennas and Propagation, Special Issue on "Communications Challenges and Dynamics for Unmanned Autonomous Vehicles," IEEE Journal on Selected Areas in Communications (JSAC), and Special Issue on "5G for Mission Critical Machine Communications", IEEE Network Magazine.